Absence of Either *Ripk3* or *Mlkl* Reduces Incidence of Hepatocellular Carcinoma Independent of Liver Fibrosis

Sabira Mohammed[1,2], Nidheesh Thadathil[2], Phoebe Ohene-Marfo[2], Albert L. Tran[2], Michael Van Der Veldt[3], Constantin Georgescu[3], Sangphil Oh[1,4], Evan H. Nicklas[2], Dawei Wang[2], Nair Hariprasad Haritha[1,2], Wenyi Luo[5], Ralf Janknecht[1,4,5], Benjamin F. Miller[6,7,8], Jonathan D. Wren[3], Willard M. Freeman[3,6,8], and Sathyaseelan S. Deepa[1,2,6,8]

ABSTRACT

Nonalcoholic fatty liver disease (NAFLD) is one of the etiologies that contribute to hepatocellular carcinoma (HCC), and chronic inflammation is one of the proposed mediators of HCC. Because necroptosis is a cell death pathway that induces inflammation, we tested whether necroptosis-induced inflammation contributes to the progression of NAFLD to HCC in a mouse model of diet-induced HCC. Male and female wild-type (WT) mice and mouse models where necroptosis is blocked (*Ripk3*$^{-/-}$ or *Mlkl*$^{-/-}$ mice) were fed either a control diet, choline-deficient low-fat diet or choline-deficient high-fat diet. Blocking necroptosis reduced markers of inflammation [proinflammatory cytokines (TNFα, IL6, and IL1β), F4/80^{+ve} macrophages, CCR2^{+ve} infiltrating monocytes], inflammation-associated oncogenic pathways (JNK, PD-L1/PD-1, β-catenin), and HCC in male mice. We demonstrate that hepatic necroptosis promotes recruitment and activation of liver macrophages leading to chronic inflammation, which in turn trigger oncogenic pathways leading to the progression of NAFLD to HCC in male mice. Whereas in female mice, blocking necroptosis reduced HCC independent of inflammation. Our data show a sex-specific difference in the development of inflammation, fibrosis, and HCC in WT mice. However, blocking necroptosis reduced HCC in both males and females without altering liver fibrosis. Thus, our study suggests that necroptosis is a valid therapeutic target for NAFLD-mediated HCC.

Implications: Necroptosis is a major contributor to hepatic inflammation that drives the progression of NAFLD to HCC and therefore represents a valid target for NAFLD-mediated HCC.

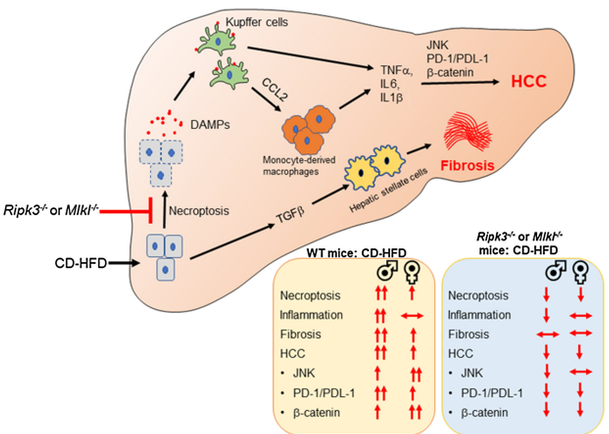

Introduction

Hepatocellular carcinoma (HCC), the primary form of liver cancer, is the fourth cancer-related cause of death worldwide with limited therapeutic options and poor survival (1). Nonalcoholic fatty liver disease (NAFLD) is one of the etiologies that contribute to HCC. NAFLD covers a spectrum of diseases ranging from fat deposition in the liver (nonalcoholic fatty liver, NAFL) to nonalcoholic steatohepatitis (NASH) that is characterized by steatosis, increased hepatic inflammation, fibrosis, and hepatocyte death. Nearly 30% of people with NAFL progress to NASH, and from these, 2%–13% progress to HCC (2). Despite the strong association between NAFLD and HCC, the pathway(s) that cause the progression of NAFLD to HCC are not clearly understood.

Nonresolving chronic inflammation is believed to be a contributor to the development and progression of HCC. One of the pathways that trigger a persistent inflammatory response is the activation of immune cells by damage-associated molecular patterns (DAMP; refs. 3, 4). DAMPs such as high mobility group box protein 1 (HMGB1) and mitochondrial DNA released from hepatocytes are proposed mediators of chronic inflammation in NASH, and levels of these DAMPs are increased in mouse models and patients with NASH (5). One of the pathways that release DAMPs from cells is necroptosis, a regulated form of inflammatory cell death (6). Necroptosis is initiated when necroptotic stimuli (e.g., TNFα, oxidative stress, lipotoxicity) sequentially activate receptor-interacting protein kinase 1 (RIPK1), RIPK3, and the pseudokinase mixed lineage kinase domain-like (MLKL) protein. Phosphorylation of MLKL leads to its oligomerization and

[1]Stephenson Cancer Center, Oklahoma City, Oklahoma. [2]Department of Biochemistry & Molecular Biology, The University of Oklahoma Health Sciences Center, Oklahoma City, Oklahoma. [3]Genes and Human Disease Research Program, Oklahoma City, Oklahoma. [4]Department of Cell Biology, The University of Oklahoma Health Sciences Center, Oklahoma City, Oklahoma. [5]Department of Pathology, The University of Oklahoma Health Sciences Center, Oklahoma City, Oklahoma. [6]Oklahoma Center for Geroscience & Brain Aging, The University of Oklahoma Health Sciences Center, Oklahoma City, Oklahoma. [7]Aging and Metabolism Research Program, Oklahoma Medical Research Foundation, Oklahoma City, Oklahoma. [8]Oklahoma City VA medical Center, Oklahoma City, Oklahoma.

Corresponding Author: Sathyaseelan S. Deepa, University of Oklahoma Health Sciences Center, Oklahoma City, OK 73104. Phone: 405-271-8001, ext. 48393; Fax: 405-271-2298; E-mail: deepa-sathyaseelan@ouhsc.edu

Mol Cancer Res 2023;21:933–46

doi: 10.1158/1541-7786.MCR-22-0820

This open access article is distributed under the Creative Commons Attribution-NonCommercial-NoDerivatives 4.0 International (CC BY-NC-ND 4.0) license.

©2023 The Authors; Published by the American Association for Cancer Research

membrane attachment, which results in permeabilization of the cell membrane and DAMP release (7). Necroptosis has been reported to be increased in the livers of NAFLD and NASH patients and in mouse models of NASH (8, 9).

Previously, we reported that inhibiting necroptosis using necrostatin-1s (Nec-1s) in a mouse model of spontaneous HCC (mice deficient in the antioxidant enzyme Cu/Zn superoxide dismutase, *Sod1*$^{-/-}$ mice) reduced hepatic inflammation, fibrosis, and pathways associated with HCC development (10). We also found that inhibiting necroptosis reduced hepatic inflammation and fibrosis in old wild-type (WT) mice that exhibit NASH pathology (11). On the basis of these findings, we hypothesized that necroptosis-mediated inflammation contributes to the progression of NAFLD to HCC. Our data show that WT male mice fed a choline-deficient amino acid–defined high-fat diet (CD-HFD) have increased inflammation, fibrosis, and HCC relative to WT female mice, and blocking necroptosis using either *Ripk3*$^{-/-}$ or *Mlkl*$^{-/-}$ mice reduced HCC in both males and females without altering liver fibrosis.

Materials and Methods

Animals and diet feeding

All procedures were approved by the Institutional Animal Care and Use Committee at the University of Oklahoma Health Sciences Center (OUHSC). Colonies of *Ripk3*$^{-/-}$ (12), *Ripk3*$^{+/+}$, *Mlkl*$^{-/-}$ (13), and *Mlkl*$^{+/+}$ mice were generated by breeding male and female *Ripk3*$^{+/-}$ or *Mlkl*$^{+/-}$ mice. The WT mice used in the study are a mix of littermates from both *Ripk3* and *Mlkl* crossings, as they do not show any difference in the parameters measured. The mice were group housed in ventilated cages at 20°C ± 2°C, 12-hour dark/light cycle. Starting at 2 months of age, male and female mice (n = 7–10/group) were fed a choline-deficient amino acid–defined diet containing 60% fat by calories (CD-HFD; A06071302i, Research Diets) for a period of 6 months at the OUHSC animal care facility. Normal chow diet (NC; 5053 Pico Lab, Purina Mills) or choline-deficient amino acid–defined diet containing 10% fat by calories (CD-LFD; A06071324i, Research diets) were used as controls (Supplementary Fig. S1A). The livers were examined for the presence of visible tumors and classified on the basis of the size and the numbers of tumors per mouse.

Western blotting

Western blotting was performed and quantified using ImageJ software (U.S. NIH) as described previously (11). The primary antibodies used were: MLKL (#MABC604) and α-smooth muscle actin (α-SMA, #A5228; Millipore Sigma), RIPK3 (#NBP1-77299, Novus Biologicals), β-tubulin (#T5201, Sigma-Aldrich), desmin (#PA5-16705, Invitrogen), P-SAPK/JNK (T183/Y185; #4668P), SAPK/JNK (#9252), P-p38 MAPK (T180/Y182; #9211S), p38 MAPK (#9212), P-p44/42 MAPK (ERK1/2; #9101S), p44/42 MAPK (ERK1/2; #4695S), β-catenin (#8480), Cyclin D1 (#2978), P-AKT (T308; #4056), AKT2 (#3063S), P-S6 ribosomal protein (S235/236; #4857), S6 ribosomal Protein (#2217), cleaved caspase-3 (#9664), and caspase-3 (#9662) from Cell Signaling Technology, p62 (#MAB8028-SP) and PD-L1 (#AF 1019) from R&D Systems. In the representative Western blots, each feeding condition per experimental group is represented by 2 independent mice. Graphical representation of the quantified Western blots for 4–6 animals/group is shown alongside the blots. In the graphs, each dot represents a mouse.

Detection of MLKL oligomers

MLKL oligomers were detected as described previously (14). Protein samples were prepared by heating with Laemmli buffer at 37°C for 15 minutes and loaded into 8% polyacrylamide gel without SDS. MLKL oligomers were detected as bands above 250 kDa using MLKL antibody.

qRT-PCR

Briefly, total RNA was isolated using RNeasy kit (# 74106, Qiagen), first-strand cDNA was synthesized using High capacity cDNA reverse transcription kit (# 4368813, Thermo Fisher Scientific), and RT-PCR using Power SYBR Green PCR Master Mix (#4368708, Thermo Fisher Scientific) in a Quantstudio 12K Flex real-time PCR system (Applied Biosystems). β-microglobulin and hypoxanthine phosphoribosyl transferase 1 (HPRT) were used as controls, as described previously (10). The list of primers used is given in Supplementary Table S3.

Characterization of immune cells by flow cytometry

Immune cell populations were analyzed by flow cytometry as described previously (15) with modifications. Briefly, mice were euthanized and liver was perfused with perfusion buffer followed by incubation in digestion buffer containing 0.075 mg/mL Liberase (#05401127001, Sigma-Aldrich). The reaction was stopped using blocking buffer, and the suspension was filtered through 70 μm cell strainer and centrifuged. The supernatant containing the non-parenchymal cells (NPC) was collected, centrifuged at 600 × g for 10 minutes, and pelleted NPC was subjected to differential centrifugation using OptiPrep density gradient media (#AXS-1114542, Cosmo Bio USA) at 1,500 × g for 30 minutes. The interphase containing NPC was collected and pelleted at 800 × g for 5 minutes. The cells were incubated with Live/Dead fixable violet dead cell stain (#L34955, Thermo Fisher Scientific) for the live cell gating and with the following antibodies from BioLegend: CD16/32 (#101302), CD45-APC/Cy7 (#103116), CD11b-PE/Cy7 (#101216), Ly6C-APC (#128016), F4/80-PE (#157304), CCR2-BV605 (#150615). Data were collected using Stratedigm 4-Laser flow cytometer, and analyzed using Flow Jo software (BD Biosciences).

Histologic analysis of liver sections

Paraffin-embedded liver sections were stained with hematoxylin & eosin (H&E) as per standardized protocol at the Stephenson Cancer Center Tissue Pathology core. Images were acquired using a Nikon Ti Eclipse microscope (Nikon) at 200× magnification for three random nonoverlapping fields per sample. Kupffer cell (KC) clusters were identified as groups of 10–12 cells clustered together and counted manually in a blinded fashion. The number of KC clusters/10 mm^2 was quantified and represented graphically.

IHC

IHC was done as described previously (16). Paraffin-embedded liver sections were incubated with primary antibodies against Glypican 3 (#MA5-17083, Thermo Fisher Scientific), Ki-67 (#ab15580, Abcam), Cleaved Caspase-3 (Cell Signaling Technology), phospho-MLKL (#ab196436, Abcam), phospho-RIPK3 (#ab205421, Abcam) overnight at 4°C. Diaminobenzidine-based colorimetric method was used for the detection of target proteins in the sections. Nuclei were counter stained with Mayer's Hematoxylin (#MHS16, Sigma-Aldrich). Images were taken using a Nikon Ti Eclipse microscope (Nikon) for three random fields per sample. Staining intensity was quantified using Image J software.

TUNEL staining

TUNEL staining was performed using paraffin-embedded liver sections (5 μm) by using the DeadEnd Colorimetric TUNEL System (#G7130, Promega) following the manufacturer's instructions.

Picrosirius red staining

Picrosirius red staining was performed with paraffin-embedded liver sections (5 μm) by following a standardized protocol at the Imaging Core facility at the Oklahoma Medical Research Foundation. Images were acquired using Nikon Ti Eclipse microscope (Nikon) for three random nonoverlapping fields per sample at 200× magnification and quantified using Image J software (U.S. NIH).

ELISA

The following ELISA kits were used to determine plasma levels of the following as per manufacturer's instructions. TNFα mouse high sensitivity ELISA kit (#BMS607-3) and IL6 mouse high sensitivity ELISA kit (#BMS603HS; Thermo Fisher Scientific), mouse CCL2/JE/MCP-1 quantikine ELISA kit (#MJE00B), mouse alpha-fetoprotein (AFP) quantikine ELISA kit (#MAFP00; R&D Systems), mouse HMGB1 ELISA Kit (#E-EL-M0676, Elabscience).

Alanine transaminase colorimetric activity assay

The levels of alanine transaminase (ALT) in plasma were measured using ALT colorimetric activity assay kit from Cayman Chemical Company (#700260) as per manufacturer's instructions.

Hydroxyproline assay

The collagen content in the liver was measured by hydroxyproline (OHP) content as described previously (17). The absorbance values at 558 nm were converted into μg units using the 4-parameter standard curve generated using the standards and expressed as μg hydroxyproline/g of tissue.

RNA sequencing and data processing

Total RNA was isolated from liver tissue using RNeasy kit (Qiagen) and library preparation was done using NEBNext Ultra II Directional RNA Library Prep Kit for Illumina (New England Biolabs; ref. 18). Paired-end 150 bp read sequencing was performed, in four to six biological replicates per diet by mouse type condition, on an Illumina NextSeq 500 sequencing platform. Raw reads, in a FASTQ format, were trimmed of residual adaptor sequences using the Scythe software. Low-quality bases at the beginning and end of reads were removed using Sickle, then the quality of remaining sequences was confirmed with FastQC. Trimmed quality reads were aligned to the *Mus musculus* genome reference (GRCm39/mm39) using STAR v2.4.0h (19). Gene-level read counts were determined using HTSeq v0.5.3p9 (20) with the GENCODE Release M29 (GRCm39) annotation. Read-count normalization and differentially expression analyses were performed using the edgeR package from Bioconductor, following the widely used limma/voom workflow (21). Differentially expressed genes were organized in expression profile sets following similar phenotype variation patterns observed in tumor incidence. Functional analysis, identifying sets of genes sharing the same functionality (Gene Ontology, Kyoto Encyclopedia of Genes and Genomes pathways), overrepresented among the differentially expressed genes, was performed with specialized packages from Bioconductor. Ingenuity Pathway Analysis (IPA, QIAGEN; https://digitalinsights.qiagen.com/products-overview/discovery-insights-portfolio/analysis-and-visualization/qiagen-ipa/?cmpid=QDI_GA_Comp&gclid=Cj0KCQjw_5unBhCMARIsACZyzS2JMPkfj3taUIlBU-laIzPAshbtyOLSmBI6nkqSYovvLHDGKwfR8bsaApXzEALw_wcB) was used further for discovery and interactive exploration of significantly impacted static and causal gene networks, pathways, disease, upstream regulators, and regulatory effects.

Statistical analysis

All data are represented as mean ± SEM. Two-way ANOVA with Tukey *post hoc* test was used to analyze data using GraphPad Prism. $P < 0.05$ is considered statistically significant. The symbols used for statistical comparison between groups are described in the figure legend.

Data availability

The data generated in this study are available within the article and its Supplementary Data. Analytic methods, and study materials will be made available to other researchers on request. Complete RNA-sequencing (RNA-seq) data are available as GSE200923 on Gene Expression Omnibus.

Results

CD-HFD increased necroptosis markers in the liver

The level of MLKL oligomers, a marker of necroptosis, were significantly increased in CD-HFD fed male (6-fold) and female WT mice (4-fold) relative to mice fed either NC or CD-LFD, and deleting *Ripk3* or *Mlkl* significantly reduced MLKL oligomerization (**Fig. 1A**). Consistent with this, levels of phospho-MLKL (22, 23) and phospho-RIPK3 were increased in the livers of mice fed CD-HFD and absence of *Ripk3* or *Mlkl* reduced the expression (**Fig. 1B**; Supplementary Fig. S1B). The increase in MLKL protein expression in WT and $Ripk3^{-/-}$ mice could be attributed to increased *Mlkl* transcript levels (**Fig. 1A**; Supplementary Fig. S1C). CD-HFD feeding increased RIPK3 protein levels in WT male mice; however, the absence of *Mlkl* blunted this effect in male mice (**Fig. 1A**). Transcript levels of *Ripk3* remained unaltered in the absence of *Mlkl* in male and female mice (Supplementary Fig. S1C). In addition, blocking necroptosis significantly reduced the elevated levels of circulating HMGB1 in male mice fed CD-HFD, though not statistically significant in females (**Fig. 1C**). Thus, increased MLKL phosphorylation and oligomerization in response to CD-HFD in WT male mice parallels elevated HMGB1 levels.

Expression of cleaved caspase-3, a marker of apoptosis, was increased in WT male mice in response to CD-LFD and CD-HFD (**Fig. 1D**; Supplementary Fig. S1D). Absence of *Ripk3* further increased cleaved caspase-3 levels whereas absence of *Mlkl* reduced its expression as shown by IHC as well as by Western blotting (**Fig. 1D**; Supplementary Fig. S1D). Though, CD-HFD increased the expression of cleaved caspase-3 in WT female mice, it was approximately 2-fold lower than in males and showed no change in $Ripk3^{-/-}$ or $Mlkl^{-/-}$ females (Supplementary Fig. S1D). To further assess cell death, TUNEL assay was performed. WT mice fed a CD-LFD or CD-HFD resulted in 3- or 6-fold increase in TUNEL positive cells, relative to WT mice fed normal chow diet. In contrast, $Ripk3^{-/-}$ and $Mlkl^{-/-}$ mice fed CD-HFD had significantly reduced TUNEL positive cells, indicating reduced cell death in the absence of *Ripk3 or Mlkl* (**Fig. 1E**). Unlike the sex-specific differences in body weight gain, no such difference was observed in liver weight in response to the diets (Supplementary Fig. S2A and S2B).

Deleting *Ripk3* or *Mlkl* reduced CD-HFD–induced inflammation in male mice

Transcript levels of *IL6*, *TNFα*, and *IL1β*, as well as circulating IL6, were significantly increased in WT male mice fed CD-HFD and were

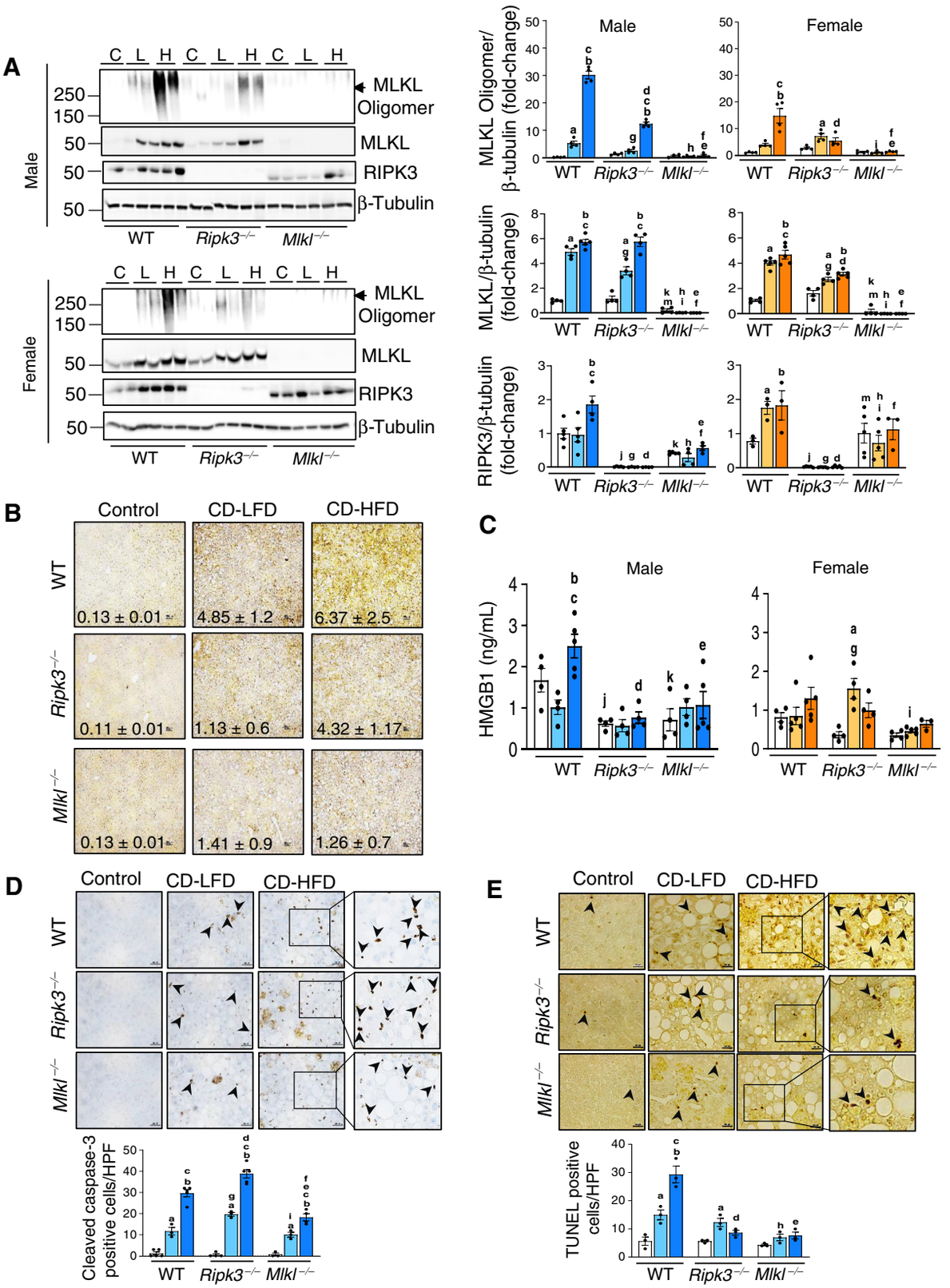
A
C L H C L H C L H
Male
250
150
50
50
50
MLKL Oligomer
MLKL
RIPK3
β-Tubulin
WT
Ripk3−/−
Mlkl−/−
Female
MLKL Oligomer/ β-tubulin (fold-change)
MLKL/β-tubulin (fold-change)
RIPK3/β-tubulin (fold-change)
B
Control
CD-LFD
CD-HFD
0.13 ± 0.01
4.85 ± 1.2
6.37 ± 2.5
0.11 ± 0.01
1.13 ± 0.6
4.32 ± 1.17
0.13 ± 0.01
1.41 ± 0.9
1.26 ± 0.7
C
HMGB1 (ng/mL)
D
Cleaved caspase-3 positive cells/HPF
E
TUNEL positive cells/HPF

significantly reduced in *Ripk3*$^{-/-}$ and *Mlkl*$^{-/-}$ mice, whereas no such effect was observed in female mice (**Fig. 2A–C**; Supplementary Fig. S2C). Circulating TNFα was elevated in both male and female WT mice fed CD-HFD, where the levels were reduced in knockout male mice, but not in female mice (**Fig. 2D**). KC clusters, a measure of the proinflammatory status of the liver (24), was significantly elevated in response to CD-LFD and CD-HFD in WT male mice, whereas blocking necroptosis reduced KC clusters in the knockout CD-HFD group (**Fig. 2E**). In WT females, though KC clusters were significantly elevated while fed with CD-HFD, this was approximately 1.5-fold lower than in male mice, and a significant reduction was seen only in *Ripk3*$^{-/-}$ group (Supplementary Fig. S2D).

The elevated levels of total immune cell population (CD45^{+ve} cells) and macrophages (F4/80^{+ve} cells), the major immune cell type mediating hepatic inflammation in response to DAMPs, increased in WT male mice fed CD-HFD and was significantly reduced in knockout male mice fed the same diet (**Fig. 3A** and **B**; Supplementary Fig. S3A). The gating strategy that was followed for the analysis is shown in Supplementary Fig S3B. In contrast to male mice, while WT females fed CD-HFD showed a significant reduction in the CD45^{+ve} population, no significant change in F4/80^{+ve} population was observed (**Fig. 3A** and **B**; Supplementary Fig. S3A). Levels of proinflammatory macrophages derived from infiltrating monocytes (CCR2^{+ve} cells; ref. 25) showed a significant increase in male WT CD-HFD group and was significantly reduced in *Ripk3*$^{-/-}$ and *Mlkl*$^{-/-}$ mice (**Fig. 3C** and **D**). Though CD-HFD fed WT female mice also had increased CCR2^{+ve} cells, their levels were approximately 2-fold lower than in males, and blocking necroptosis had no effect on these cells in females (**Fig. 3C** and **D**).

Transcript levels of chemokine (C-C motif) ligand 2 (*CCL2*), a chemokine that recruits monocytes to the sites of injury (25), were significantly increased in WT mice in response to CD-HFD and these levels were significantly reduced in *Ripk3*$^{-/-}$ and *Mlkl*$^{-/-}$ mice (**Fig. 3E**). Similarly, circulating CCL2 was elevated in response to CD-HFD in WT male and female mice; however, CCL2 levels were significantly reduced in *Ripk3*$^{-/-}$ and *Mlkl*$^{-/-}$ males, but not in females (**Fig. 3F**). Also, the markers of proinflammatory M1 macrophages, *CD68* and *TLR4*, elevated in WT male mice fed CD-HFD were significantly reduced in knockout groups (Supplementary Fig. S3C).

Blocking necroptosis did not alter CD-HFD–induced liver fibrosis

CD-HFD feeding resulted in severe fibrosis as seen by the increased intensity in PicroSirius red (PSR) staining of liver tissue which was not reduced when necroptosis was blocked. Moreover, the staining intensity was higher in males (∼3-fold) than in females (**Fig. 4A**). The increased transcript levels of *Col3α1*, *Acta2*, and *Col1α1* in WT males fed with CD-HFD (**Fig. 4B** and **C**; Supplementary Fig. S4A) was reduced when *Ripk3* was absent. Whereas, only *Col1α1* showed a significant reduction in *Mlkl*$^{-/-}$ mice fed CD-HFD, in males and females (**Fig. 4B** and **C**; Supplementary Fig. S4A). Assessment of hepatic stellate cell (HSC) markers showed that desmin and α-SMA increased in WT CD-HFD were reduced only in male *Ripk3*$^{-/-}$ mice (**Fig. 4D**; Supplementary Fig. S4B). *TGFβ* transcript levels were significantly upregulated in WT mice fed CD-HFD and blocking necroptosis had no effect on *TGFβ* levels in male or female mice (**Fig. 4E**; Supplementary Fig. S4C). Similarly, OHP which was significantly elevated in the livers of WT male mice fed CD-LFD and CD-HFD were not reduced in knockout males (**Fig. 4F**). Circulating levels of ALT, a biomarker of hepatocellular damage, were also significantly elevated in WT male mice in response to CD-LFD and CD-HFD and the levels did not change significantly in the knockout groups (**Fig. 4G**).

Deleting either *Ripk3* or *Mlkl* significantly reduced HCC development in response to CD-HFD

WT male mice fed CD-HFD developed liver nodules (2–25 nodules/mouse) while no or few liver nodules were detected in mice fed NC or CD-LFD (**Fig. 5A**; Supplementary Fig. S5A). While a similar effect was observed in female mice, the number of liver nodules was lower (∼2- to 3-fold) relative to males (**Fig. 5A**). Importantly, the number and size of liver nodules were significantly reduced in both *Ripk3*$^{-/-}$ and *Mlkl*$^{-/-}$ male and female mice fed CD-HFD (**Fig. 5A** and **B**; **Table 1**). The tumor (T) region of liver sections from CD-HFD fed WT mice showed strong positive staining for glypican-3, a marker for HCC, (**Fig. 5C**) as well as the cell proliferation marker, Ki-67, compared with non-tumor (NT) region and this was reduced in both *Ripk3*$^{-/-}$ and *Mlkl*$^{-/-}$ mice (**Fig. 5D**). The elevated levels of serum AFP, a biomarker of HCC, in WT mice fed CD-HFD were significantly reduced in the knockout groups (**Fig. 5E**). Transcript levels of liver AFP also showed a similar trend for males, but not for females (Supplementary Fig. S5B).

Gene expression modulation in response to CD-LFD or CD-HFD was attenuated when necroptosis is blocked

To determine the effect of blocking necroptosis on the liver transcriptome of male mice, RNA-seq was performed. The transcriptomic changes in WT mice induced by CD-LFD and CD-HFD feeding was largely prevented in the *Ripk3*$^{-/-}$ and *Mlkl*$^{-/-}$ groups (**Fig. 6A**). A list of the transcripts that significantly changed is given in Supplementary Tables S1 and S2. To validate the RNA-seq data, we performed qRT-PCR analysis of selected genes associated with tumorigenesis that were altered in WT mice fed CD-HFD: *Tonsl* (26), *Dppa2* (27), and *Pogz* (28). The mRNA levels of these genes were significantly increased in WT mice fed CD-HFD and blocking necroptosis reduced their expression (**Fig. 6B**).

Further analysis by IPA identified 24 pathways that were significantly altered (Supplementary Fig. S6A) and of these, pathways that showed positive (necroptosis signaling pathway and senescence pathway), and negative (sirtuin signaling pathway and CLEAR signaling pathway) z-score are showed in **Fig. 6C**. WT male mice fed CD-HFD showed increase in markers of senescence, *p16*, *p21* and *p53*, compared with control. p21 was significantly reduced in *Ripk3*$^{-/-}$ and *Mlkl*$^{-/-}$

Figure 1.

CD-HFD increased necroptosis in liver and deleting either *Ripk3* or *Mlkl* reduced necroptosis. **A,** Left: Immunoblots of liver tissue extracts for MLKL oligomers, MLKL, RIPK3, and β-tubulin from WT, *Ripk3*$^{-/-}$, and *Mlkl*$^{-/-}$ male (top) and female (bottom) mice fed NC (C), CD-LFD (L) or CD-HFD (H). Right: Graphical representation of quantified blots normalized to β-tubulin. Males: NC (white), CD-LFD (light blue) or CD-HFD (dark blue). Females: NC (white), CD-LFD (light orange) or CD-HFD (dark orange). **B,** IHC staining for P-MLKL in liver sections from WT, *Ripk3*$^{-/-}$, and *Mlkl*$^{-/-}$ male mice fed NC or CD-LFD or CD-HFD. The intensity of staining was quantified and represented. Scale bar: 25 μm. **C,** HMGB1 in plasma of WT, *Ripk3*$^{-/-}$, and *Mlkl*$^{-/-}$ male (left) and female (right) mice. **D,** Top: IHC staining for cleaved caspase-3 in liver sections from male mice. Bottom: Graphical representation of number of cleaved caspase-3 positive cells per high-power field (HPF). Scale bar: 50 μm. **E**, Top: TUNEL staining in liver sections from male mice. Bottom: Graphical representation of number of TUNEL positive cells per HPF. Scale bar: 50 μm. Arrowheads indicate positive cells. For **Figs. 1–7**, data are represented as mean ± SEM, $n = 4–6$ per group, Two-way ANOVA $P < 0.05$. a-NC versus CD-LFD, b-NC versus CD-HFD, c-CD-LFD versus CD-HFD. Between groups: j-WT NC versus *Ripk3*$^{-/-}$ NC, k-WT NC versus *Mlkl*$^{-/-}$ NC, m-*Ripk3*$^{-/-}$ NC versus *Mlkl*$^{-/-}$ NC, g-WT CD-LFD versus *Ripk3*$^{-/-}$ CD-LFD, h-WT CD-LFD versus *Mlkl*$^{-/-}$ CD-LFD, i-*Ripk3*$^{-/-}$ CD-LFD versus *Mlkl*$^{-/-}$ CD-LFD, d-WT CD-HFD versus *Ripk3*$^{-/-}$ CD-HFD, e-WT CD-HFD versus *Mlkl*$^{-/-}$ CD-HFD, f-*Ripk3*$^{-/-}$ CD-HFD versus *Mlkl*$^{-/-}$ CD-HFD.

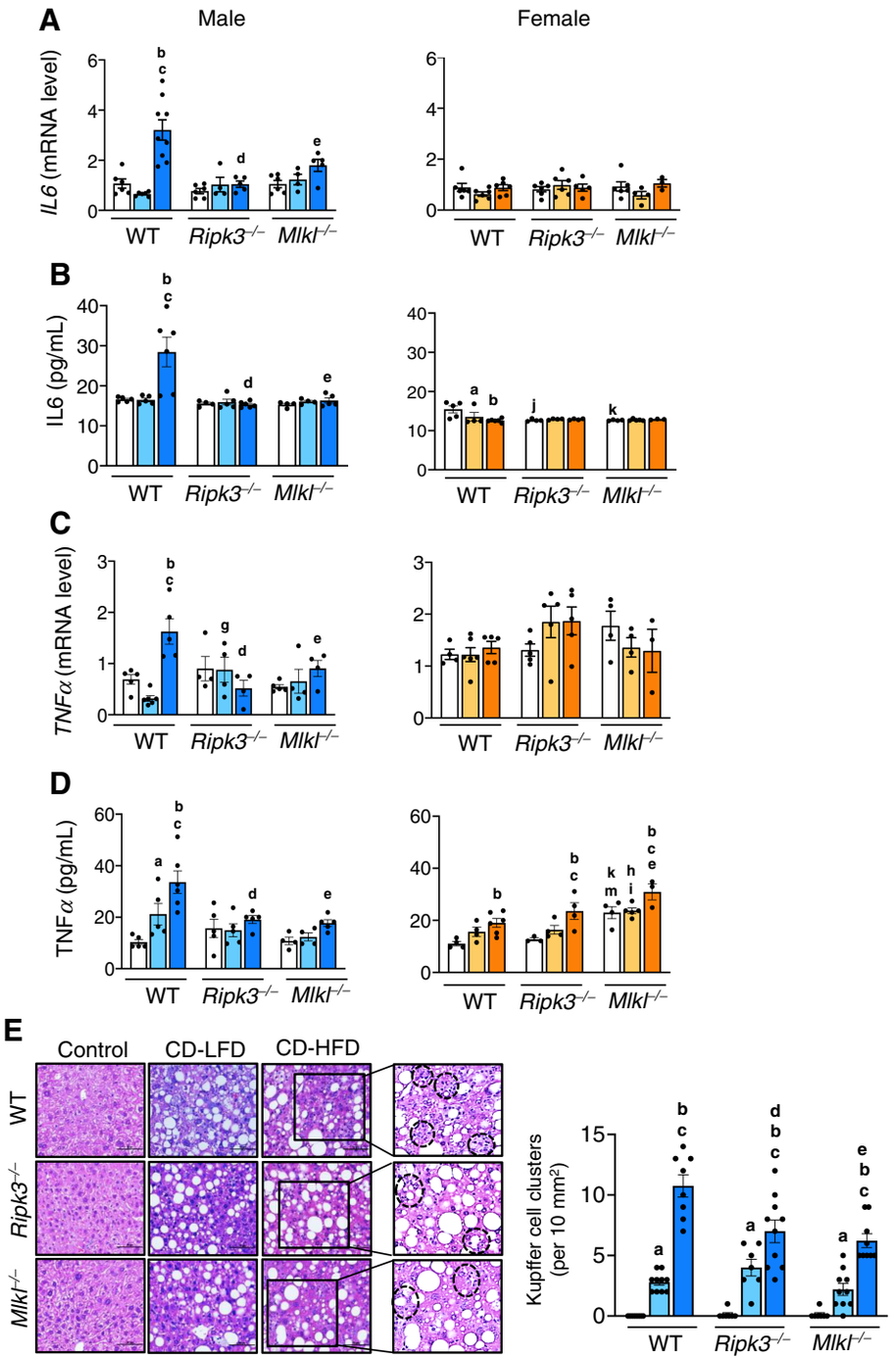

Figure 2.

Deleting *Ripk3* or *Mlkl* reduced CD-HFD induced inflammation in male mice. Transcript levels of hepatic *IL6* (**A**), circulating IL6 (**B**), transcript levels of hepatic *TNFα* (**C**), and circulating TNFα (**D**) in male (left) and female (right) mice. **E,** Left: Images of H&E stained sections. Black dotted circles represent KC clusters. Scale bar: 50 μm. Right: Graphical representation of the number of KC clusters in each group. Males: NC (white), CD-LFD (light blue) or CD-HFD (dark blue). Females: NC (white), CD-LFD (light orange) or CD-HFD (dark orange).

male mice fed CD-HFD, whereas p16 and p53 was significantly reduced only in *Ripk3*$^{-/-}$ group (**Fig. 6D**). In WT female mice, *p16* and *p21*, but not *p53*, were significantly elevated in response to CD-HFD and blocking necroptosis reduced their expression in *Mlkl*$^{-/-}$ mice, but not in *Ripk3*$^{-/-}$ mice (**Fig. 6D**). IPA further identified 15 upstream regulators of the pathways (Supplementary Fig. S6B), of which one showed a positive z-score (STAT5) and two showed negative z-score (LEP and PPARα; **Fig. 6E**).

Oncogenic pathways induced by CD-HFD is attenuated when necroptosis is blocked

To identify pathways mediating HCC development in response to CD-HFD, the activation of HCC-associated pathways was assessed. Male mice were used for the initial studies and the pathways that were found to be activated in males were then validated in females. We assessed MAPK pathways that are modulated by inflammation and are involved in HCC, for example, JNK, ERK and p38 pathways, by

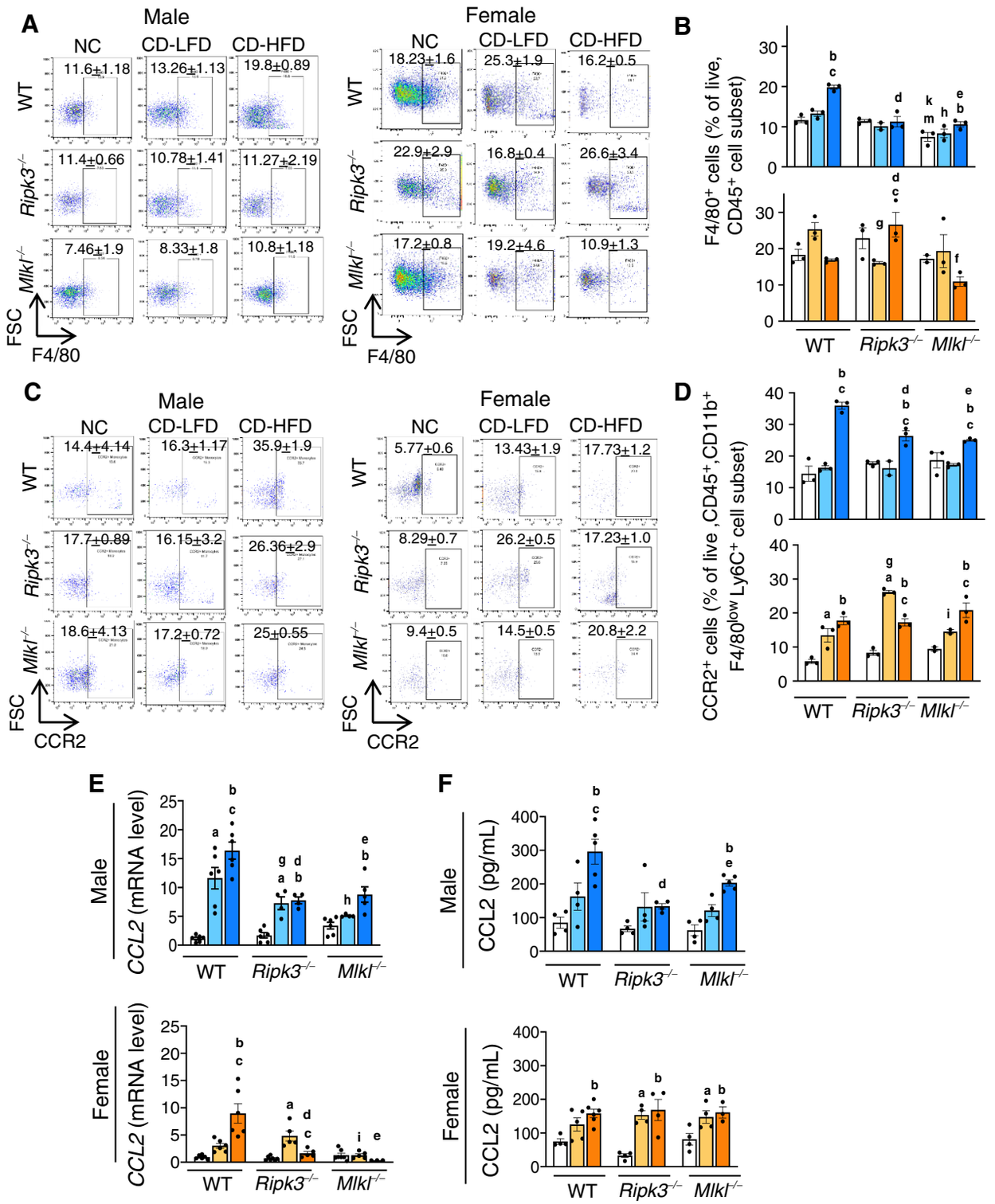

Figure 3.

Deleting *Ripk3* or *Mlkl* reduced CD-HFD–induced CCL2 and CCR2^{+ve} macrophages. Left: Flow cytometric analysis of percentage of F4/80^{+ve} cell population (**A**) and CCR2^{+ve} cell population (**C**) in the livers of male (left) and female (right) mice. Right: Graphical representation of the percentage population of F4/80^{+ve} cells gated on liver CD45^{+ve} cell subset (**B**) and CCR2^{+ve} cells, gated on liver CD45^{+}, CD11b^{+}, F4/80^{low}, Ly6C^{+}, Ly6G^{-} cell subsets (**D**) in male (top) and female (bottom) mice. Transcript levels of hepatic *CCL2* (**E**) and circulating CCL2 (**F**). Males: NC (white), CD-LFD (light blue) or CD-HFD (dark blue). Females: NC (white), CD-LFD (light orange) or CD-HFD (dark orange).

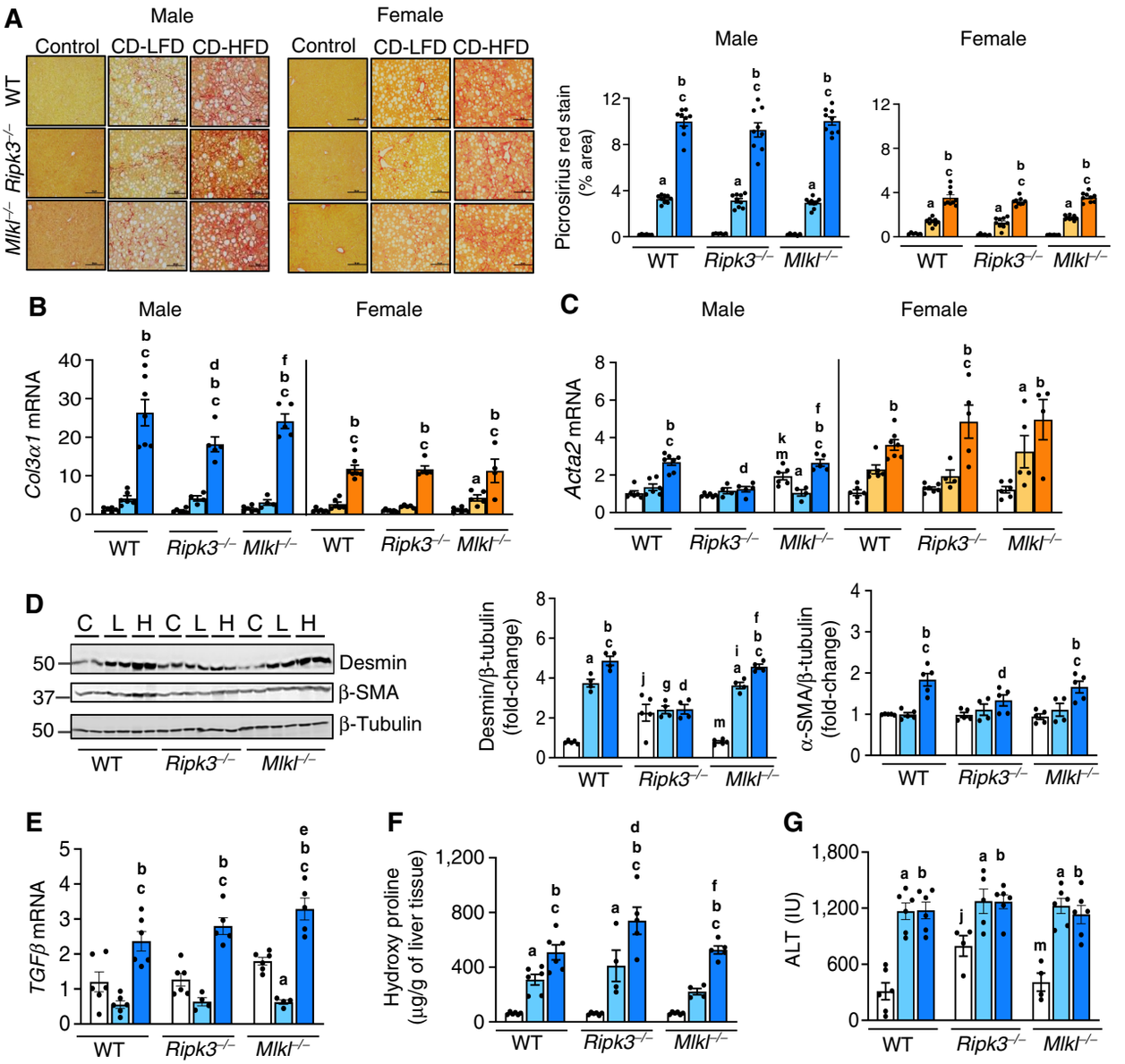

Figure 4.

Deleting either *Ripk3* or *Mlkl* did not alter liver fibrosis. **A,** Left: PSR staining of liver sections of male (left) and female (right) mice. Scale bar: 50 µm. Right: Graphical representation of PSR quantification. Transcript levels of *Col3α1* (**B**) and *Acta2* (**C**) in male (left) and female mice (right). **D,** Left: Immunoblots of liver tissue extracts for desmin, α-SMA, and β-tubulin from male mice fed NC (C) or CD-LFD (L) or CD-HFD (H). Right: Graphical representation of quantified blots normalized to β-tubulin. Transcript levels of hepatic *TGFβ* normalized to β-microglobulin (**E**), liver hydroxyproline content (**F**), and serum ALT levels (**G**). Males: NC (white), CD-LFD (light blue) or CD-HFD (dark blue). Females: NC (white), CD-LFD (light orange) or CD-HFD (dark orange).

assessing phosphorylation levels of these proteins which represent the active form. Phosphorylation of JNK was increased in the livers of CD-HFD fed WT mice, and was significantly reduced in knockout male mice, but not in females (**Fig. 7A**). The AKT/mTOR and p38 pathways were not activated in WT male mice fed CD-HFD, whereas ERK phosphorylation was reduced and remained unaltered in knockout mice (Supplementary Fig. S7A and S7B).

The elevated levels of β-catenin and its downstream target, cyclin D1, in CD-HFD fed WT male mice were significantly reduced in knockout groups (**Fig. 7B**). Similarly, blocking necroptosis reduced β-catenin expression in females in response to CD-HFD (Supplementary Fig. S7C). Also, transcript levels of *c-Myc* and *EpCAM*, the downstream targets of the JNK and β-catenin pathways, elevated in WT male mice fed CD-HFD was significantly reduced in knockout groups (**Fig. 7C**). Interestingly, the increased expression of PD-L1, the immune checkpoint protein, which was significantly upregulated in the livers of WT male mice fed CD-HFD was reduced in both knockout groups fed CD-HFD with a greater reduction in *Mlkl*$^{-/-}$ group (**Fig. 7D**). Similarly, transcript levels of *PD-L1* and *PD-1* in the liver were increased in male and female WT mice in response to CD-HFD,

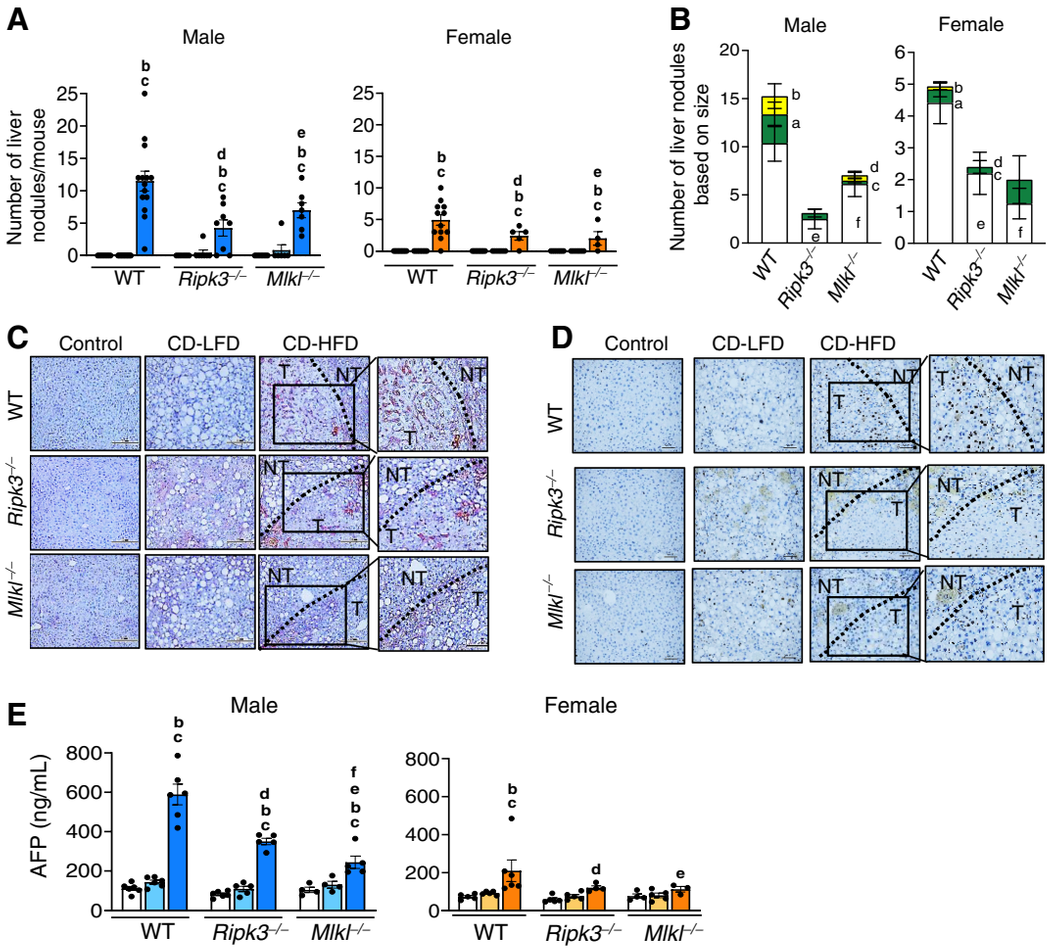

Figure 5.

Deleting either *Ripk3* or *Mlkl* significantly reduced HCC in response to a CD-HFD. **A,** Tumor nodules in the livers of WT, *Ripk3*$^{-/-}$, and *Mlkl*$^{-/-}$ male mice (left) and female mice (right). **B,** Graphical representation of large (>5 mm, yellow), medium (2–4 mm, green), and small (<1 mm, white) liver nodules in male (left) and female (right) mice [[a]WT small tumor (ST) vs. WT medium tumor (MT), $P < 0.0001$; [b]WT ST vs. WT large tumor (LT), $P < 0.0001$; [c]*Mlkl*$^{-/-}$ ST vs. *Mlkl*$^{-/-}$ MT, $P < 0.01$; [d]*Mlkl*$^{-/-}$ ST vs. *Mlkl*$^{-/-}$ LT, $P < 0.01$; [e]WT ST vs. *Ripk3*$^{-/-}$ ST, $P < 0.0001$; [f] WT ST vs. *Mlkl*$^{-/-}$ ST, $P < 0.03$]. IHC staining for glypican-3 (**C**) and Ki-67 (**D**) in the non-tumor (NT) and tumor (T) of liver sections from male mice. Dark red color in tumor (T) region indicate positive staining for glypican-3 and dark brown spots in tumor region indicate positive staining for Ki-67. Scale bar: 50 μm. **E,** Circulating AFP levels male (left) and female (right) mice. Males: NC (white), CD-LFD (light blue) or CD-HFD (dark blue). Females: NC (white), CD-LFD (light orange) or CD-HFD (dark orange).

and were significantly reduced in all knockout groups fed CD-HFD (**Fig. 7E**). Furthermore, similar to previous reports (29), we found *PPARγ* to be significantly upregulated in *Ripk3*$^{-/-}$ and *Mlkl*$^{-/-}$ mice fed CD-HFD compared with WT group, thereby underlining the role of necroptotic proteins in PPARγ modulation (**Fig. 7F**). Also, p62, a marker of autophagy that is elevated in HCC, was significantly upregulated in WT male mice fed CD-HFD with no change seen in the knockout groups (Supplementary Fig. S7D).

Table 1. Tumor incidence and size-based indication of tumors in the experimental groups.

	Males			Females		
	WT	***Ripk3*$^{-/-}$**	***Mlkl*$^{-/-}$**	**WT**	***Ripk3*$^{-/-}$**	***Mlkl*$^{-/-}$**
Tumor incidence	100% (10/10)	75% (6/8)	100% (7/7)	87.5% (7/8)	80% (4/5)	75% (3/4)
Small sized tumors: <0.1 mm (number and percentage)	10.36 ± 1.86, 68%	2.86 ± 1.01, 80%	6.14 ± 1.32, 87%	4.42 ± 0.66, 90%	2.2 ± 0.66, 92%	1.25 ± 0.48, 64%
Medium sized tumors: 2–4 mm (number and percentage)	3 ± 1.27, 20%	0.625 ± 0.42, 20%	0.33 ± 0.21, 5%	0.42 ± 0.23, 9%	0.2 ± 0.2, 8%	0.75 ± 0.7, 36%
Large sized tumors: >5 mm (number and percentage)	1.88 ± 1.28, 12%	0 0	0.57 ± 0.297, 8%	0.1 ± 0.1, 2%	0,0	0,0

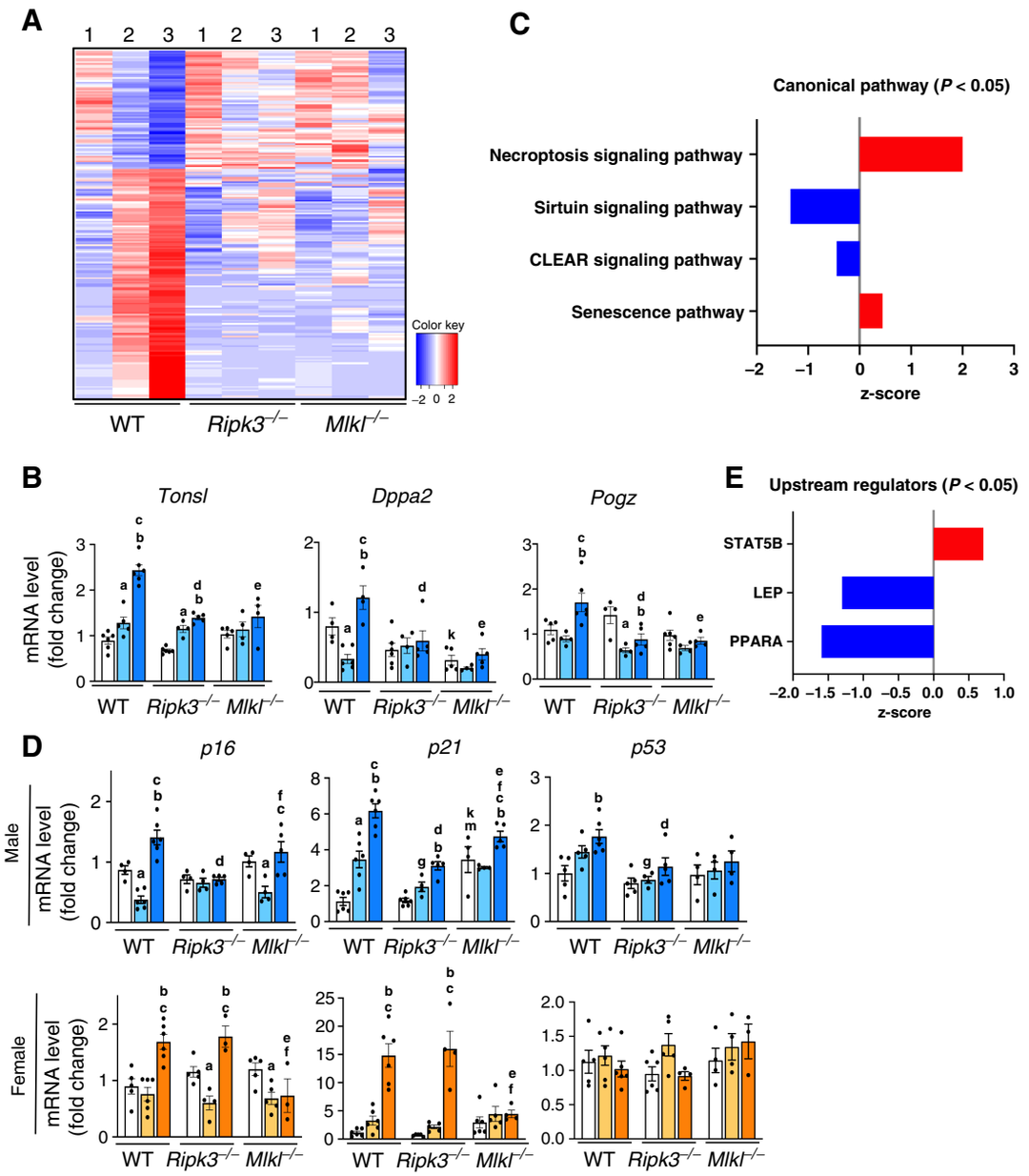

Figure 6.

Genes upregulated or downregulated in response to CD-LFD or CD-HFD in WT, *Ripk3*$^{-/-}$ or *Mlkl*$^{-/-}$ mice. **A,** Schematic representation of transcriptome analysis of liver tissue extracts. Red color represents genes that are significantly upregulated and blue color represents genes that are significantly downregulated (1: NC, 2: CD-LFD, 3: CD-HFD). **B,** Transcript levels of *Tonsl*, *Dppa2*, and *Pogz* normalized to β-microglobulin in male mice. **C,** Graphical representation of canonical pathways which are significantly upregulated (red) and downregulated (blue). **D,** Transcript levels of *p16*, *p21,* and *p53* in male (top) and female (bottom). **E,** Upstream regulators that are significantly upregulated (red) and downregulated (blue) in male mice. Males: NC (white), CD-LFD (light blue) or CD-HFD (dark blue). Females: NC (white), CD-LFD (light orange) or CD-HFD (dark orange).

Discussion

This study addressed the role of two key proteins in the necroptosis pathway, RIPK3 and MLKL, on hepatic inflammation and HCC development in a NASH-induced HCC mouse model; and the sex-specific effects of deleting *Ripk3* or *Mlkl* on inflammation, liver fibrosis, and HCC. The major findings of the study are that deleting either *Ripk3* or *Mlkl* ameliorated hepatic inflammation and HCC in male mice and HCC only in female mice. Liver fibrosis was however not improved in either male or female mice. By showing that both *Ripk3* and *Mlkl* knockout mice had similar effects on reducing inflammation and/or HCC in response to CD-HFD, we propose that necroptosis plays a role in HCC induction in the CD-HFD mouse model.

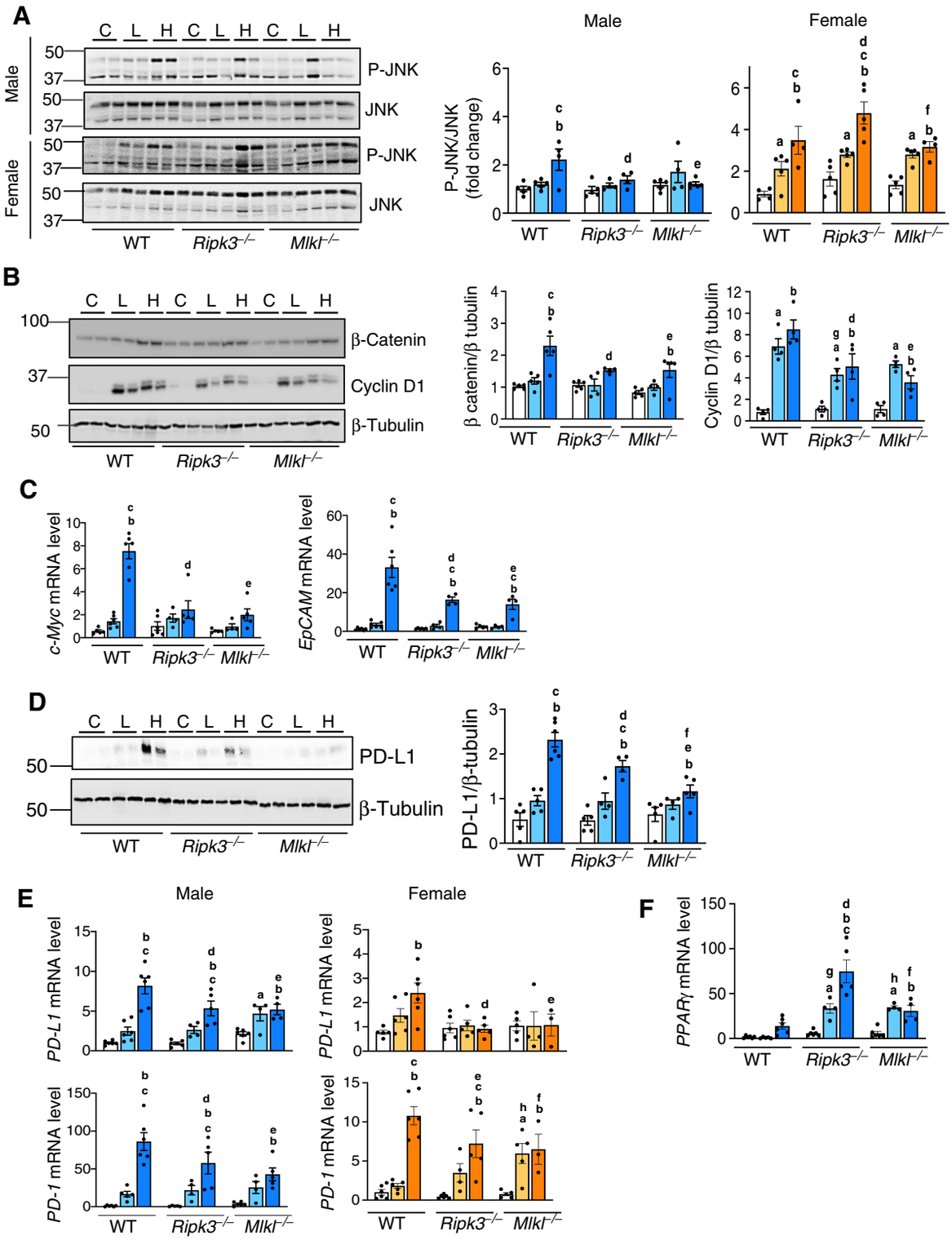

Figure 7.

Changes in pathways involved in HCC. **A,** Left: Immunoblots of liver tissue extracts for P-JNK and JNK male (top) and female (bottom) mice fed NC (C), CD-LFD (L) or CD-HFD (H). Right: Graphical representation of quantified phosphoprotein normalized to total protein. **B,** Immunoblots of liver tissue extracts for β-catenin, cyclin-D1 and β-tubulin (left) from male mice. Right: Graphical representation of quantified blots normalized to β-tubulin. **C,** Transcript levels of *c-Myc* (left) and *EpCAM* (right). **D,** Left: Immunoblots of liver tissue extracts for PD-L1 and β-tubulin. Right: Graphical representation of quantified blots normalized to β-tubulin. Transcript levels of (**E**) hepatic *PD-L1* (top) and *PD-1* (bottom), and (**F**) *PPARγ* normalized to β-microglobulin. Males: NC (white), CD-LFD (light blue) or CD-HFD (dark blue). Females: NC (white), CD-LFD (light orange) or CD-HFD (dark orange).

Our study agrees with previous reports showing increased necroptosis in the livers of male mice fed NAFLD or NASH inducing diets (8, 29, 30). While the absence of *Mlkl* abolished MLKL oligomer levels, deletion of *Ripk3* reduced MLKL oligomer levels, suggesting a role of TAM (Tyro3, Axl, and Mer) kinases in MLKL phosphorylation and oligomerization (31). Liver macrophages, in particular the infiltrating monocyte-derived macrophages, are the major mediators of the inflammatory response in NASH and HCC (32). Our finding that blocking necroptosis reduced total liver macrophages and infiltrating monocytes suggests a role for liver macrophages in necroptosis-mediated inflammation in male WT mice, not female mice. The female sex hormone, estrogen, has been shown to inhibit production of proinflammatory cytokines by KC (33), and male mice is reported to accumulate more macrophages in the adipose tissue than females leading to elevated levels of inflammatory cytokines (34). Although female mice fed CD-HFD had increased levels of necroptosis markers, neither HMGB1 nor proinflammatory cytokines were elevated, suggesting that plasma membrane rupture, the terminal step in necroptosis is inhibited in females. Future studies will determine whether MLKL oligomers are ubiquitinated to block the cytotoxic potential in female mice (35).

Oncogenic pathways regulated by inflammatory cytokines are increased in the livers of WT male mice fed CD-HFD, that is, JNK, PD-L1/PD-1, and β-catenin pathways (36–38). Deleting either *Ripk3* or *Mlkl* reduced JNK, PD-1/PD-L1 signaling, and β-catenin pathways in male mice, supporting a role of necroptosis-mediated inflammation in HCC in male mice. These pathways were also elevated in WT female mice fed CD-HFD, but blocking necroptosis reduced only PD-1/PD-L1 signaling and β-catenin pathways, suggesting other factors in addition to necroptosis-mediated inflammation can modulate these pathways. Our study also confirms the role of RIPK3 in NASH progression to HCC, where the expression of RIPK3 in human NASH subjects negatively correlates with PPARγ expression (29), thereby suggesting the role of necroptotic proteins in controlling the hepatic lipid metabolism, and hence NASH incidence.

Absence of *Ripk3* or *Mlkl* reduced the number and size of liver tumor nodules in male and female mice. Even though WT female mice developed HCC in response to CD-HFD, the number of tumor nodules were approximately 2.5-fold lower than in WT male mice, consistent with the fact that HCC incidence in humans is >2-fold higher in males than females (39). Similarly, diethylnitrosamine-induced hepatocarcinogenesis model had shown higher incidence of HCC in males relative to females (33). Surprisingly, though blocking necroptosis reduced liver tumor nodules in females, the reduction occurred in the absence of any significant decrease in inflammation. This finding suggests the existence of alternate pathways regulated by both *Ripk3* and *Mlkl* in HCC development in females.

Chronic liver inflammation is a well-known mediator of liver fibrosis (40). Even though the increase in hepatic inflammation was paralleled by increased liver fibrosis in male mice fed CD-HFD, deleting neither *Ripk3* nor *Mlkl* had any effect on liver fibrosis suggesting that necroptosis-mediated inflammation does not play a role in liver fibrosis. Contrary to our findings, deleting *Ripk3* reduced hepatic inflammation and liver fibrosis in male mice fed methionine- and choline-deficient diet or choline-deficient diet (8, 29). Also, feeding *Ripk3*$^{-/-}$ mice with HFD exacerbated hepatic inflammation and liver fibrosis (22, 41). Similarly, *Ripk3* deletion is protective, whereas *Ripk1* inhibition aggravated disease and hastened animal death in ConA-induced autoimmune hepatitis (42). It is possible that discrepancies in dietary fat sources as well as the composition in diets or compounds used to induce chronic liver disease is the cause of different outcomes. Our data show that deleting neither *Ripk3* nor *Mlkl* had any effect on the elevated levels of TGFβ, the fibrogenic factor involved in the activation of HSCs. Similar to humans, liver fibrosis was observed to be higher in male mice relative to females (43). A role for the female sex hormone, estrogen, has been proposed for the gender differences in liver fibrosis and HCC based on the finding that the degree of liver fibrosis and HCC are higher in postmenopausal women than in premenopausal women (44).

Our study identified a novel cross-talk between necroptosis and other pathways that regulate tumorigenesis, for example, apoptosis and cell senescence. Deletion of *Ripk3* elevated apoptosis markers as reported previously (29), whereas *Mlkl* deficiency reduced apoptosis, suggesting that reduction of HCC is independent of apoptosis. Recently, we reported that inhibiting necroptosis using Nec-1s reduced markers of cell senescence in the livers of *Sod1*$^{-/-}$ mice, a mouse model of spontaneous HCC, as well as in the livers of old WT mice (11, 45), further supporting a role of necroptosis in cell senescence. As cell senescence also regulates inflammation, it is possible that the observed outcome of HCC inhibition in both *Ripk3*$^{-/-}$ and *Mlkl*$^{-/-}$ mice could also be due to inhibition of both necroptosis and cellular senescence (46).

The novel aspects of our study are: (i) To our knowledge, this is the first study showing a protective role of MLKL deficiency on HCC in response to CD-HFD. Even though a previous study has reported that absence of *Ripk3* could reduce HCC (29), the study used a choline-deficient amino acid–defined diet that lacks high fat. (ii) Our study shows that reduced incidence of HCC due to *Ripk3* or *Mlkl* deficiency is independent of fibrosis. (iii) RIPK3 and MLKL regulate cellular processes other than necroptosis: RIPK3 modulates apoptosis, NLRP3 activation, and lipid metabolism (29, 47), whereas MLKL regulates autophagy and endosomal trafficking (48, 49). Therefore, similar outcomes using both *Ripk3*$^{-/-}$ and *Mlkl*$^{-/-}$ mouse models in our study suggest involvement of necroptosis. Ours is the only study that tested effect of *Ripk3* or *Mlkl* deletion in males and females simultaneously to show a sex-specific difference.

In summary, our data provide strong support for necroptosis playing a role in HCC in a mouse model of NASH-induced HCC. In addition, our study offers insight into sex-specific differences in the progression of NASH to HCC, demonstrating the need for using both males and females for studies, especially for developing therapeutic strategies for treating HCC. As HCC incidence is higher in postmenopausal women relative to premenopausal women (50), the study also highlights the importance of using estrogen-deficient female mice for studying HCC.

Authors' Disclosures

No disclosures were reported.

Authors' Contributions

S. Mohammed: Data curation, formal analysis, investigation, methodology, writing–review and editing. **N. Thadathil:** Data curation, formal analysis, investigation, methodology, writing–review and editing. **P. Ohene-Marfo:** Formal analysis, investigation, methodology, writing–review and editing. **A.L. Tran:** Formal analysis, investigation, methodology, writing–review and editing. **M. Van Der Veldt:** Formal analysis, investigation. **C. Georgescu:** Formal analysis, investigation, writing–review and editing. **S. Oh:** Formal analysis, writing–review and editing. **E.H. Nicklas:** Formal analysis, investigation, writing–review and editing. **D. Wang:** Formal analysis, investigation. **N.H. Haritha:** Formal analysis, investigation, writing–review and editing. **W. Luo:** Formal analysis, writing–review and editing. **R. Janknecht:** Formal analysis, writing–review and editing. **B.F. Miller:** Formal analysis, writing–review and editing. **J.D. Wren:** Formal analysis, writing–review and editing. **W.M. Freeman:** Formal analysis, writing–review and editing. **S.S. Deepa:** Conceptualization, formal

analysis, supervision, funding acquisition, writing–original draft, project administration, writing–review and editing.

Acknowledgments

The efforts of authors were supported by NIH grants R01AG059718 (S.S. Deepa), R03 CA262044 (S.S. Deepa), P30AG050911(W.M. Freeman, J.D. Wren, and B.F. Miller), R01 AG064951 (B.F. Miller), R56 AG067754 (B.F. Miller), R21 AR077387 (B. F. Miller), P20 GM139763 (B.F. Miller), GeroOncology Pilot Grant (R. Janknecht and S.S. Deepa) from the University of Oklahoma Health Sciences Center, Oklahoma Center for Adult Stem Cell Research Grant (OCASCR; S.S. Deepa) and Oklahoma Center for the Advancement of Science and Technology (OCAST) Postdoctoral grant HF21-009 (S. Mohammed).

The authors would like to thank Stephenson Cancer Center Tissue Pathology Core for performing H&E staining, the Imaging Core facility at the Oklahoma Medical Research Foundation for performing Picrosirius red, cleaved caspase-3 and TUNEL staining, and the Laboratory for Molecular Biology and Cytometry Research at the University of Oklahoma Health Sciences Center for providing the facilities for the flow cytometry experiments.

The publication costs of this article were defrayed in part by the payment of publication fees. Therefore, and solely to indicate this fact, this article is hereby marked "advertisement" in accordance with 18 USC section 1734.

Note

Supplementary data for this article are available at Molecular Cancer Research Online (http://mcr.aacrjournals.org/).

Received October 17, 2022; revised April 13, 2023; accepted May 16, 2023; published first May 19, 2023.

References

1. Llovet JM, Kelley RK, Villanueva A, Singal AG, Pikarsky E, Roayaie S, et al. Hepatocellular carcinoma. Nat Rev Dis Prim 2021;7:6.
2. Huang DQ, El-Serag HB, Loomba R. Global epidemiology of NAFLD-related HCC: trends, predictions, risk factors and prevention. Nat Rev Gastroenterol Hepatol 2021;18:223–38.
3. Yu LX, Ling Y, Wang HY. Role of nonresolving inflammation in hepatocellular carcinoma development and progression. NPJ Precis Oncol 2018;2:6.
4. Mihm S. Danger-associated molecular patterns (DAMPs): molecular triggers for sterile inflammation in the liver. Int J Mol Sci 2018;19:3104.
5. Gaskell H, Ge X, Nieto N. High-mobility group box-1 and liver disease. Hepatol Commun 2018;2:1005–20.
6. Newton K, Manning G. Necroptosis and inflammation. Annu Rev Biochem 2016;85:743–63.
7. Samson AL, Zhang Y, Geoghegan ND, Gavin XJ, Davies KA, Mlodzianoski MJ, et al. MLKL trafficking and accumulation at the plasma membrane control the kinetics and threshold for necroptosis. Nat Commun 2020;11:3151.
8. Gautheron J, Vucur M, Reisinger F, Cardenas DV, Roderburg C, Koppe C, et al. A positive feedback loop between RIP3 and JNK controls non-alcoholic steatohepatitis. EMBO Mol Med 2014;6:1062–74.
9. Gautheron J, Vucur M, Schneider AT, Severi I, Roderburg C, Roy S, et al. The necroptosis-inducing kinase RIPK3 dampens adipose tissue inflammation and glucose intolerance. Nat Commun 2016;7:11869.
10. Mohammed S, Nicklas EH, Thadathil N, Selvarani R, Royce GH, Kinter M, et al. Role of necroptosis in chronic hepatic inflammation and fibrosis in a mouse model of increased oxidative stress. Free Radic Biol Med 2021;164:315–28.
11. Mohammed S, Thadathil N, Selvarani R, Nicklas EH, Wang D, Miller BF, et al. Necroptosis contributes to chronic inflammation and fibrosis in aging liver. Aging Cell 2021;20:e13512.
12. Newton K, Sun X, Dixit VM. Kinase RIP3 is dispensable for normal NF-kappa Bs, signaling by the B-cell and T-cell receptors, tumor necrosis factor receptor 1, and Toll-like receptors 2 and 4. Mol Cell Biol 2004;24:1464–9.
13. Murphy JM, Czabotar PE, Hildebrand JM, Lucet IS, Zhang JG, Alvarez-Diaz S, et al. The pseudokinase MLKL mediates necroptosis via a molecular switch mechanism. Immunity 2013;39:443–53.
14. Miyata T, Wu X, Fan X, Huang E, Sanz-Garcia C, Cajigas-Du Ross CK, et al. Differential role of MLKL in alcohol-associated and non-alcohol-associated fatty liver diseases in mice and humans. JCI insight 2021;6:e140180.
15. Stijlemans B, Sparkes A, Abels C, Keirsse J, Brys L, Elkrim Y, et al. Murine liver myeloid cell isolation protocol. Bio-Protocol 2015;5:e1471.
16. Lankadasari MB, Aparna JS, Mohammed S, James S, Aoki K, Binu VS, et al. Targeting S1PR1/STAT3 loop abrogates desmoplasia and chemosensitizes pancreatic cancer to gemcitabine. Theranostics 2018;8:3824–40.
17. Smith LR, Hammers DW, Sweeney HL, Barton ER. Increased collagen cross-linking is a signature of dystrophin-deficient muscle. Muscle Nerve 2016;54:71–8.
18. Ocañas SR, Pham KD, Blankenship HE, Machalinski AH, Chucair-Elliott AJ, Freeman WM. Minimizing the ex vivo confounds of cell-isolation techniques on transcriptomic and translatomic profiles of purified microglia. eNeuro 2022;9:ENEURO.0348-21.2022.
19. Dobin A, Davis CA, Schlesinger F, Drenkow J, Zaleski C, Jha S, et al. STAR: ultrafast universal RNA-seq aligner. Bioinformatics 2013;29:15–21.
20. Anders S, Pyl PT, Huber W. HTSeq–a python framework to work with high-throughput sequencing data. Bioinformatics 2015;31:166–9.
21. Law CW, Chen Y, Shi W, Smyth GK. voom: precision weights unlock linear model analysis tools for RNA-seq read counts. Genome Biol 2014;15:R29.
22. Roychowdhury S, McCullough RL, Sanz-Garcia C, Saikia P, Alkhouri N, Matloob A, et al. Receptor interacting protein 3 protects mice from high-fat diet-induced liver injury. Hepatology 2016;64:1518–33.
23. Wu X, Nagy LE. MLKL contributes to western diet-induced liver injury through inhibiting autophagy. Autophagy 2020;16:1351–2.
24. Woltman AM, Boonstra A, Naito M, Leenen PJM. Kupffer cells in health and disease. Macrophages: biology and role in the pathology of diseases. New York (NY): Springer; 2014. p. 217–47.
25. Zimmermann HW, Trautwein C, Tacke F. Functional role of monocytes and macrophages for the inflammatory response in acute liver injury. Front Physiol 2012;3:56.
26. Yu B, Ding Y, Liao X, Wang C, Wang B, Chen X. Overexpression of TONSL might be an independent unfavorable prognostic indicator in hepatocellular carcinoma. Pathol Res Pract 2019;215:939–45.
27. Monk M, Hitchins M, Hawes S. Differential expression of the embryo/cancer gene ECSA(DPPA2), the cancer/testis gene BORIS and the pluripotency structural gene OCT4, in human preimplantation development. Mol Hum Reprod 2008;14:347–55.
28. Zheng S, Liu Y, Sun H, Jia J, Wu T, Ding R, et al. Identification of abnormally high expression of POGZ as a new biomarker associated with a poor prognosis in osteosarcoma. Eur J Histochem 2021;65:3264.
29. Afonso MB, Rodrigues PM, Mateus-Pinheiro M, Simão AL, Gaspar MM, Majdi A, et al. RIPK3 acts as a lipid metabolism regulator contributing to inflammation and carcinogenesis in non-alcoholic fatty liver disease. Gut 2021;70:2359–72.
30. Afonso MB, Rodrigues PM, Carvalho T, Caridade M, Borralho P, Cortez-Pinto H, et al. Necroptosis is a key pathogenic event in human and experimental murine models of non-alcoholic steatohepatitis. Clin Sci 2015;129:721–39.
31. Najafov A, Mookhtiar AK, Luu HS, Ordureau A, Pan H, Amin PP, et al. TAM kinases promote necroptosis by regulating oligomerization of MLKL. Mol Cell 2019;75:457–68.
32. Daemen S, Schilling JD. The interplay between tissue niche and macrophage cellular metabolism in obesity. Front Immunol 2019;10:3133.
33. Naugler WE, Sakurai T, Kim S, Maeda S, Kim KH, Elsharkawy AM, et al. Gender disparity in liver cancer due to sex differences in MyD88-dependent IL-6 production. Science 2007;317:121–4.
34. Chen K-HE, Lainez NM, Coss D. Sex differences in macrophage responses to obesity-mediated changes determine migratory and inflammatory traits. J Immunol 2021;206:141–53.
35. Liu Z, Dagley LF, Shield-Artin K, Young SN, Bankovacki A, Wang X, et al. Oligomerization-driven MLKL ubiquitylation antagonizes necroptosis. EMBO J 2021;40:e103718.
36. Kuntzen C, Sonuc N, De Toni EN, Opelz C, Mucha SR, Gerbes AL, et al. Inhibition of c-Jun-N-terminal-kinase sensitizes tumor cells to CD95-induced apoptosis and induces G_2–M cell cycle arrest. Cancer Res 2005;65:6780–8.

37. Khalaf AM, Fuentes D, Morshid AI, Burke MR, Kaseb AO, Hassan M, et al. Role of wnt/β-catenin signaling in hepatocellular carcinoma, pathogenesis, and clinical significance. J Hepatocell Carcinoma 2018;5:61–73.
38. Singh V, Khurana A, Allawadhi P, Banothu AK, Bharani KK, Weiskirchen R. Emerging role of PD-1/PD-L1 inhibitors in chronic liver diseases. Front Pharmacol 2021;12:790963.
39. Wu EM, Wong LL, Hernandez BY, Ji JF, Jia W, Kwee SA, et al. Gender differences in hepatocellular cancer: disparities in nonalcoholic fatty liver disease/steatohepatitis and liver transplantation. Hepatoma Res 2018;4:66.
40. Koyama Y, Brenner DA. Liver inflammation and fibrosis. J Clin Invest 2017;127:55–64.
41. Saeed WK, Jun DW, Jang K, Ahn SB, Oh JH, Chae YJ, et al. Mismatched effects of receptor interacting protein kinase-3 on hepatic steatosis and inflammation in non-alcoholic fatty liver disease. World J Gastroenterol 2018;24:5477–90.
42. Deutsch M, Graffeo CS, Rokosh R, Pansari M, Ochi A, Levie EM, et al. Divergent effects of RIP1 or RIP3 blockade in murine models of acute liver injury. Cell Death Dis 2015;6:e1759.
43. Ballestri S, Nascimbeni F, Baldelli E, Marrazzo A, Romagnoli D, Lonardo A. NAFLD as a sexual dimorphic disease: role of gender and reproductive status in the development and progression of nonalcoholic fatty liver disease and inherent cardiovascular risk. Adv Ther 2017;34:1291–326.
44. Ascha MS, Hanouneh IA, Lopez R, Tamimi TAR, Feldstein AF, Zein NN. The incidence and risk factors of hepatocellular carcinoma in patients with nonalcoholic steatohepatitis. Hepatology 2010;51:1972–8.
45. Thadathil N, Selvarani R, Mohammed S, Nicklas EH, Tran AL, Kamal M, et al. Senolytic treatment reduces cell senescence and necroptosis in Sod1 knockout mice that is associated with reduced inflammation and hepatocellular carcinoma. Aging Cell 2022;21:e13676.
46. Giannakoulis VG, Dubovan P, Papoutsi E, Kataki A, Koskinas J. Senescence in HBV-, HCV- and NAFLD- mediated hepatocellular carcinoma and senotherapeutics: current evidence and future perspective. Cancers 2021;13:4732.
47. Moriwaki K, Chan FKM. The inflammatory signal adaptor RIPK3: functions beyond necroptosis. Int Rev Cell Mol Biol 2017;328:253–75.
48. Wu X, Poulsen KL, Sanz-Garcia C, Huang E, McMullen MR, Roychowdhury S, et al. MLKL-dependent signaling regulates autophagic flux in a murine model of non-alcoholic fatty liver disease. J Hepatol 2020;73:616–27.
49. Yoon S, Kovalenko A, Bogdanov K, Wallach D. MLKL, the protein that mediates necroptosis, also regulates endosomal trafficking and extracellular vesicle generation. Immunity 2017;47:51–65.
50. Zhang W, Liu F, Huang J, Guo X, Dong W, Wei S, et al. Effect of menopausal status on the survival and recurrence of sex-classified hepatocellular carcinoma after liver resection: a case-matched study with propensity score matching. Aging 2020;12:25895–915.